Application of bipolar electrochemistry to assess the ambient temperature corrosion resistance of solution annealed type 2205 duplex stainless steel

DOI:
10.1016/j.matchemphys.2021.125183

Document Version
Accepted author manuscript

Application of bipolar electrochemistry to assess the ambient temperature corrosion resistance of solution annealed type 2205 duplex stainless steel

Yiqi Zhou[*1], *Dirk Lars Engelberg*[1,2]

(1) Corrosion & Protection Centre, Department of Materials, The University of Manchester, M13 9PL, Manchester, UK

(2) Materials Performance Centre, The University of Manchester, M13 9PL, Manchester, UK

* Corresponding author: Yiqi.zhou@postgrad.manchester.ac.uk

Abstract

The corrosion resistance of solution annealing heat-treated type 2205 duplex stainless steel microstructures was assessed with a bipolar electrochemistry technique. Chemical element partitioning in both crystallographic phases was correlated to simulations of critical pitting temperatures. The as-received microstructure had the highest pit nucleation resistance, with high-temperature solution annealing treatment revealing reduced pit growth rates. Pit nucleation occurred either within the ferrite phase or at ferrite-austenite interfaces, with the resulting pit shape affected by the microstructure characteristics. The results of this study are discussed in the framework of microstructure design for enhanced corrosion resistance in duplex stainless steels.

Keywords: Bipolar electrochemistry, corrosion, duplex stainless steel, pitting, solution annealing.

Introduction

Duplex stainless steels (DSS) are generally chosen for critical applications based on their excellent mechanical properties, superior corrosion resistance compared to most other stainless steels, and their unrivalled crack propagation resistance [1–3]. In the solution annealed microstructure condition, DSS only consist of ferrite (α) and austenite (γ) [4,5]. The ferrite typically provides stiffness and chloride-induced stress corrosion cracking (SCC) resistance, with the austenite contributing ductility and hydrogen embrittlement (HE) resilience.

The occurrence of pitting corrosion in stainless steels is linked to a heterogeneous breakdown of the passive surface film, followed by highly localised metal dissolution via metastable and stable pit growth [6,7]. Most work on pit initiation and growth has been undertaken on austenitic and ferritic stainless steels, with metastable pits showing the presence of characteristic lacy metal covers, which act as diffusion limiting barrier. These barriers then result in the accumulation of increased anion concentrations within pits [8,9]. Transition to stable pit growth typically results via the loss of these lacy covers, with the overall pit depth and morphology then acting as diffusion limiting parameter [10,11]. The shape and topography of pits is therefore an important factor in determining growth characteristics and associated kinetic behaviour.

In DSS, the localised corrosion resistance is more complex as different elements partition to the different crystallographic phases present, with ferrite generally becoming enriched in Cr and Mo, and the austenite in Ni, Mn, and N. The chemical fingerprint of each phase facilitates the corrosion characteristics, with the pitting corrosion behaviour typically limited by the weaker ferrite phase [12,13]. Changes in the ferrite-to-austenite volume fraction typically comes with a redistribution of alloying elements within the two phases. The latter redistribution can be achieved, for example, via application of solution annealing heat treatments with the aim to optimise the corrosion resistance and

associated mechanical properties without introducing further deleterious phases [14–17].

In contrast, the heat affect zone (HAZ) of DSS 2205 (22%Cr-5%Ni) has also been associated with reduced corrosion resistance, based on adversely distributed alloying elements in both the ferrite and austenite phase [18]. For DSS 2205 and Super DSS 2507 (25%Cr-7%Ni), the highest critical pitting temperature (CPT) is achieved when both the ferrite and austenite have the same pitting resistance equivalent number (PREN). From ASTM G48 Method E, the CPT (°C) is calculated by CPT = 2.5 × %Cr + 7.6 × %Mo + 31.9 × %N – 41, with the PREN assessed via PREN = %Cr + 3.3 × %Mo+ 30 × %N [19]. These equations point towards a key influence of three main alloying elements (Cr, Mo and N), positively affecting pitting corrosion resistance. However, for lean DSS 2101 (21%Cr-1%Ni), an optimized PREN between ferrite and austenite cannot be achieved by heat treatments [20]. Lower temperature annealing treatment might precipitate other phases, such as sigma phase, chi phase, and chromium nitride, which all reduce the corrosion resistance [21–23]. Heat treatment applied to duplex stainless steel can also affect stress corrosion cracking behaviour, with the presence of Cr-oxides and hydrogen embrittlement-related crack path features observed by an in-operando x-ray computed microtomography study [24].

Bipolar electrochemistry provides access to the full spectrum of anodic-to-cathodic electrochemical reactions in a single experiment [25]. The non-contact setup provides a rapid experimental outcome, with this method typically used for corrosion screening of stainless steels from 2013 [26,27], and then the corrosion behaviour of welded duplex stainless, austenitic stainless steel, ferritic stainless steel are tested by bipolar electrochemistry [28–31]. The corrosion behaviour of type 420 ferritic stainless steel from bipolar electrochemistry, 3-electrode potentiodynamic and potentiostatic polarisation test in 0.1M HCl are investigated and compared [32]. Furthermore, bipolar

electrochemistry is applied on the brass dezincification studies and galvanic corrosion test [33,34].

Bipolar electrochemistry was used to test the pitting corrosion resistance of type 2205 duplex stainless steel at room temperature and also used to research the relationship between the heat treatment and pitting corrosion for martensitic stainless steel [30,35]. In the work reported here, different solution annealing heat treatments for DSS 2205 are applied, to demonstrate application of bipolar electrochemistry to probe the localised corrosion resistance under a wide range of heat treatment conditions. To avoid the formation of harmful secondary phase such as σ and χ (that are known to make the microstructure susceptible to corrosion) only treatment s from 1000°C and above should be chosen [36]. Solution heat treatment of grade 2205 duplex stainless steel is usually carried out above 1000°C, with applied temperatures typically up to with 1350°C explored [37,38]. Here, our manuscript used a solution treatment temperature range from 1000°C to 1350°C, with bipolar electrochemistry applied to assess and compare the pitting corrosion resistance of all microstructure at room temperature. The results are discussed in the framework of pit nucleation and propagation to design enhanced DSS microstructures.

Materials and Methods

A standard grade 2205 DSS in the solution annealed as received (AR) microstructure condition was used in this study. The material had a chemical composition of (wt.%) 22.4 Cr, 0.016 C, 0.4 Si, 5.8 Ni, 1.5 Mn, 3.3 Mo, 0.16 N, and Fe (bal.), with a PREN of 38.4, and an estimated CPT of 45 °C (ASTM G48). Heat treatments were performed at 1000 °C, 1150 °C, 1250 °C, 1300 °C, and 1350 °C in a CWF chamber furnace. The samples were held for 1 hour at the set temperature, followed by rapid cooling in water.

For bipolar electrochemistry testing, all bipolar electrodes (BPEs) had a dimension of 30 x 10 x 2 mm^3 (length x width x thickness). All samples were prepared by grinding with SiC paper from 400 to 1200 grit, followed by polishing to a 1 µm diamond paste finish. For EBSD analysis, the samples were further polished to 0.25 µm diamond paste finish, followed by an OPS Colloidal Silica (OPS) fine polish.

A schematic set-up of the bipolar set-up is shown in Figure 1 (a), by using a Keysight E36105A as power source. A galvanostatic current of 1 A was applied between the feeder electrodes, which were set at a distance of 6 cm apart. The BPE was at the centre of the two Pt feeder electrodes, which had each a surface area of 4 cm^2. All bipolar experiments were run in 200 ml of 0.1M HCl for a duration of 900 seconds. To measure the acting potential along the BPE, a conductive wire was electric connected to the rear of the BPE, with a saturated calomel electrode (SCE) in a Luggin capillary as reference electrode. Measurements were carried out at a set distance of ≈ 1mm above the BPE surface. The local potential changes on the BPE were measured by recording first the open circuit potential (OCP), followed by switching on the Keysight power supply to initiate the bipolar electrochemistry set-up. Figure 1(b) gives the difference of potentials measured along the BPE electrode with applied bipolar electrochemistry, giving the average potential over the first 600 seconds. A quasi-linear potential gradient is observed along the centre-line of the BPE, with a slightly increased potential responses near the BPE oxidation edge, and a more negative response close to the BPE reduction edge.

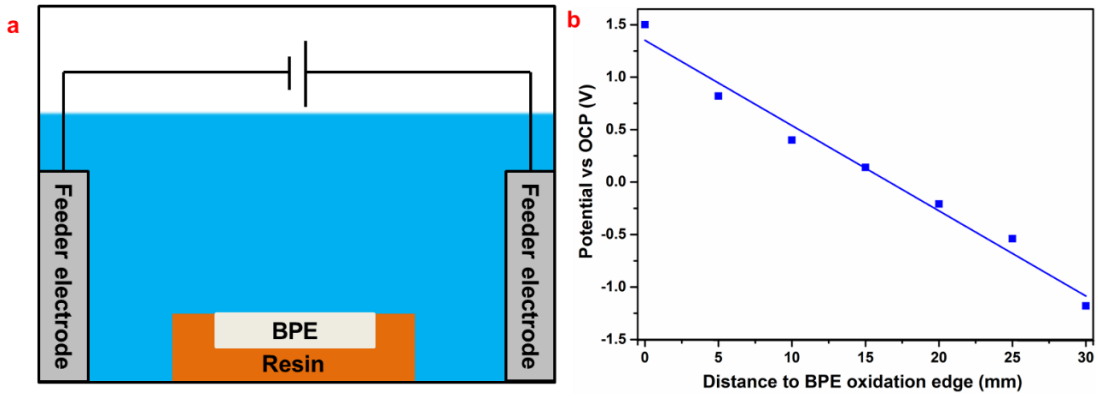

Figure 1 (a) Schematic setup of the bipolar electrochemistry experiment, and (b) measured potential distribution along the BPE (potential change vs OCP).

For 3-electrode potentio-dynamic polarisation, an AVESTA cell with 0.1M HCl solution was used. All experiments were carried out at room temperature, by using a Pt counter with SCE reference electrode. An IVIUM-Compactstat with IVIUMsoft software was then used to measure potentio-dynamic polarisation curves. At first the OCP was measured for 600 seconds, followed by conducting potentio-dynamic polarisation tests starting from -0.2 V_{OCP} to +1.2 V_{OCP} by using a scan rate of 1 mV/s.

After concluding all corrosion tests, samples were washed in soap water and dried in hot air. The corrosion topography was obtained with a Keyence VK-200K laser scanning confocal microscope, with measured regions having a width of 4 mm. SEM imaging and EDX analysis was carried out in a Zeiss Sigma VP FEG-SEM at 20 kV, using Aztec software for analysis. Electron Backscatter Diffraction (EBSD) was carried out in a Sirion FEG-SEM and Zeiss Sigma VP FEG-SEM at 20 kV, with a step size of 0.14 µm and 3.8 µm, respectively. The small step size was employed over typical areas of 125.5 x 93.2 μm^2, to inform about the presence of other crystallographic phases, with the large step size applied to characterise the size and distribution of ferrite vs. austenite.

Result and Discussion

Microstructure Characterisation

The microstructures of the wrought as received and all solution annealing heat-treated samples are summarised in Figure 2. The microstructures only contained ferrite and austenite, with no other visible precipitates or tertiary phases present. The microstructures were also inspected for the potential presence of quench-in chromium nitrides (CrN), which can form during rapid cooling. No signs of quench-in CrN were found.

In the AR specimen and the sample annealed at 1000 ºC, the austenite phase is evenly distributed in the form of elongated islands within the ferritic matrix. Both microstructures had along the rolling direction elongated ferrite- and austenite-containing regions, showing typical ribbon-like morphologies of wrought DSS microstructure. The island-shaped austenite grains grow larger, whereas ferrite grains become wider gradually as the annealing temperature increases up to 1250 ºC. For specimens annealed at temperature in excess of 1250 ºC, the microstructure developed a different morphology. As the microstructure transforms into ferrite at such temperature, the austenitic phase dissolves and reforms through a solid-state phase transformation during the cooling process. High temperature heat treatments then produce ferritic grains, surrounded by reformed secondary austenite. The cooling rate then affects the overall composition of both phases, with further cooling then also resulting in intragranular or plate-like Widmansstaetten austenite needles. Grain boundary austenite is present in Figure 2 (e,f), with Widmanstaetten austenite found after the 1350 ºC annealing treatment in Figure 2 (f).

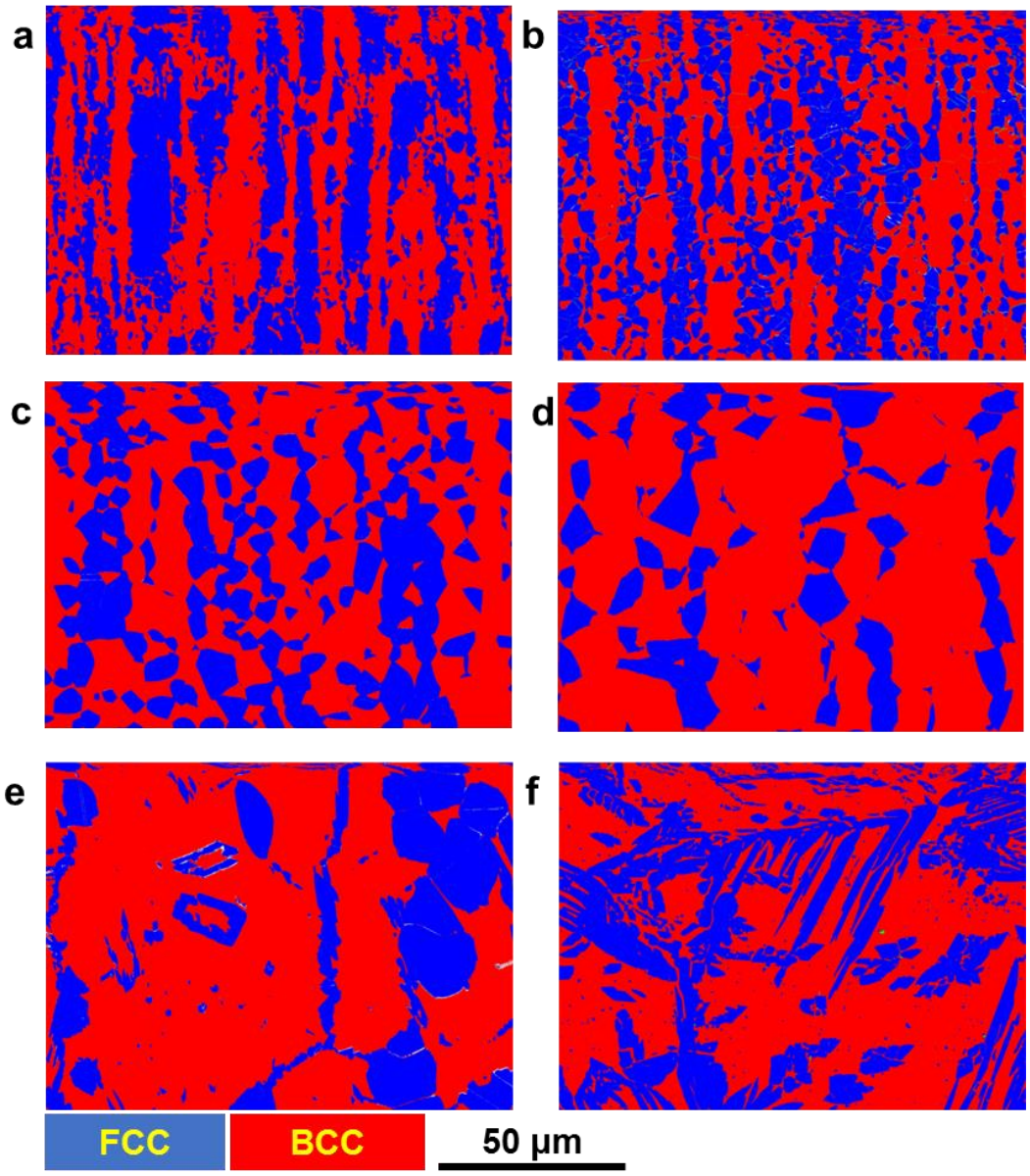

Figure 2 The EBSD of DSS 2205 with different heat treatment temperature, from (a) AR, (b) 1000 ^{o}C, (c) 1150 ^{o}C, (d) 1250 ^{o}C, (e) 1300 ^{o}C, to (f) 1350 ^{o}C, with the latter showing Widmannstaetten austenite needles.

The diameter of the austenite and ferrite phase regions at different temperatures is shown in Figure 3 (a). Both phase diameters become larger at higher annealing temperature, with the austenite-to-ferrite transformation resulting in significant differences in grain diameters. For specimen heat treated below 1250 ^{o}C, the grain size in both ferrite and austenite phase are monotonically increasing with increasing temperature, due to the balanced

distribution of both phases. However, for specimen heat treated over 1300 ^{o}C, the ferrite size is significantly increased, due to the high temperature transformation of austenite into δ-ferrite. Longer heat treatment at these temperatures can intermittently produce fully ferritic microstructures [39]. The resulting grain size has been reported to influence the overall corrosion behaviour, with for example, DSS 2202 (22%Cr-2%Ni) showing higher current densities potentio-static polarisation tests with larger grain sizes [40]. Figure 3 (b) summarises the change in ferrite to austenite phase fraction with annealing temperature, supporting all previous observations of the effect of annealing temperature on the phase transformations. For specimens annealed at 1350 ^{o}C, the final ferrite concentration reduces, as more austenite reforms due to far longer diffusion times for elements during the heat treatment and cooling schedule.

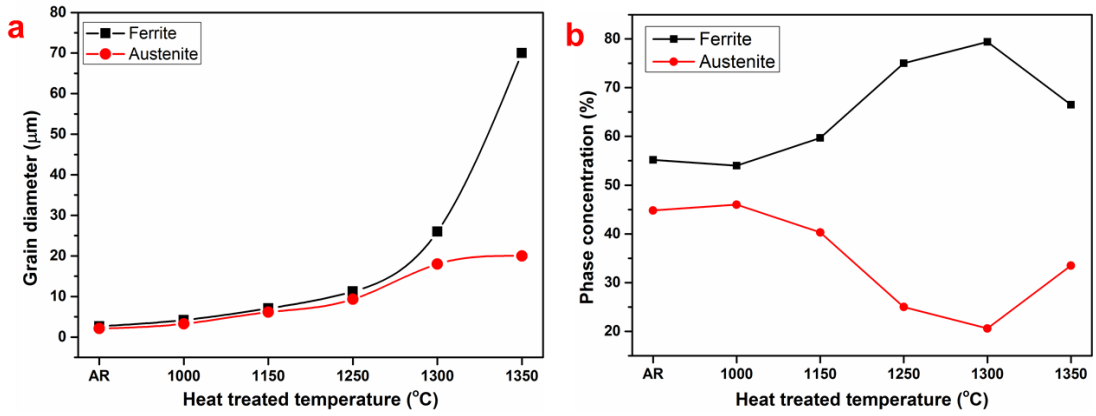

Figure 3 (a) Average diameter ferrite and austenite grain size and (b) concentration of ferrite and austenite phase

Figure 4 gives large area EBSD maps of specimen annealed at 1300 ^{o}C and 1350 ^{o}C. The specimen annealed at 1350 ^{o}C produces coarse grained ferrite that favoured the formation of austenite in specific areas. Austenite has three locations and morphologies, (i) a continuous phase at prior-ferrite grain boundaries, (ii) acicular-type Widmanstätten plates growing into ferrite grains,

(iii) and discrete intragranular regions. At a relatively high annealing temperatures, the concentration of grain boundary allotriomorphs austenite and the Widmänstten austenite increased significantly. Many of the intragranular austenite grains reveal significant grain growth to assume more spheroidal shapes. It is also observed that the austenite grains do not exhibit any preferred growth direction.

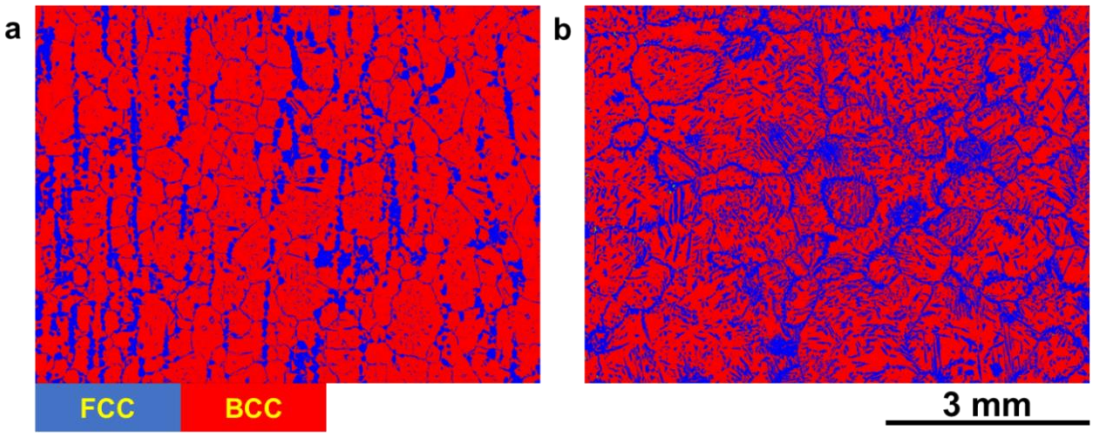

Figure 4 The EBSD of DSS 2205 at a low magnification after heat treated at (a) 1300 ^{o}C and (b) 1350 ^{o}C.

Element Partitioning & PREN

The concentrations of the three major alloying elements Cr, Ni, and Mo as a function of annealing temperature are listed in Table 1. Ten random EDX measurements at each phase have been obtained and the mean value is calculated with the standard deviation. For specimen annealed below 1250 ^{o}C, both Cr and Mo are enriched in the ferrite, whereas Ni is concentrated in the austenite phase. With higher annealing temperatures, the concentration of Cr and Mo in the ferrite phase decreases, with the Ni increasing; at the same time, the concentration of Cr and Mo in the austenite slightly increases. For specimen annealed over 1300 ^{o}C, the three key elements Cr, Ni, and Mo are balanced in both the ferrite and austenite phase. The alloying elements diffuse relatively slowly in the solid state; hence, they cannot partition between ferrite and austenite.

Table 1 Alloying elements contents of tested specimens.

	Phase	Cr	Ni	Mo
AR	BCC	24.5±0.2	4.7±0.1	4.3±0.1
	FCC	21.8±0.4	7.0±0.2	2.8±0.2
1000 °C	BCC	25.1±0.2	4.1±0.2	4.7±0.2
	FCC	21.6±0.2	7.0±0.2	2.9±0.1
1150 °C	BCC	24.2±0.2	4.8±0.1	4.3±0.1
	FCC	21.7±0.5	7.2±0.1	2.9±0.1
1250 °C	BCC	23.3±0.2	4.7±0.2	4.2±0.3
	FCC	21.6±0.3	6.8±0.3	3.2±0.3
1300 °C	BCC	23.3±0.1	5.6±0.1	4.1±0.1
	FCC	23.1±0.2	6.0±3.0	3.9±0.2
1350 °C	BCC	22.4±0.1	5.8±0.1	4.1±0.1
	FCC	22.1±0.5	6.5±0.2	3.5±0.2

Figure 5 plots data from Table 1, highlighting differences between ferrite and austenite elemental compositions. The largest difference is present for specimen annealed at 1000 °C, and then reduces with increasing annealing temperature, reaching a minimum for samples annealed at 1300-1350 °C, the corrosion behaviour of each phase is related to the chemical composition, which was revealed by scanning kelvin probe force microscopy (SKPFM). The larger the difference of Cr, Mo, and Ni within the two phases, the higher was the observed Volta potential difference between the two phases, resulting in lower corrosion resistance [18]. These observations are also supported by PREN and CPT simulations, with the CPT calculated from ASTM G48 Method E. Table 1 provides data to simulation the expected PREN and CPT values for each phase, with the concentration of nitrogen assumed to reach saturateion in the ferrite. The latter is assumed to reach a maximum of 0.05% N, with the rest then partitioned into the austenite phase. Here we do not consider the possibility of nitrogen loss during the annealing treatment [37,41].

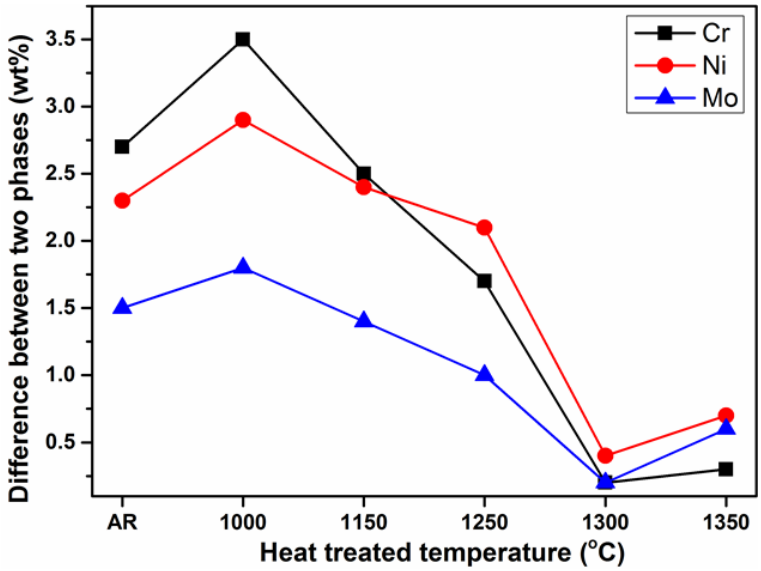

Figure 5 The main alloying elements difference between two phases after difference annealed temperatures.

Figure 6 shows the CPT and PREN of the ferrite and austenite at different heat treatment temperatures. The austenite phase has typically higher PREN values except for the 1000 ^{o}C annealed sample. Pits are therefore expected to nucleate in the ferrite phase, with the pitting corrosion resistance (the weaker PREN phase) following 1000 ^{o}C > AR > 1150 ^{o}C > 1250 ^{o}C > 1300 ^{o}C > 1350 ^{o}C. Two distinct groups are apparent in Figure 6, with all high temperature treatments 1250-1350 ^{o}C having far higher PREN in the ferrite, compared to the lower temperature treatments, but the inverse was observed for the austenite; here the lower temperature treatments had higher PREN values.

In contrast for the CPT simulations, the ferrite phase indicated a higher CPT for heat treatments lower than 1150 ^{o}C, but for heat treatments at 1250 ^{o}C and above, the austenite phase had a higher CPT. The pitting corrosion resistance according to CPT calculations (lower CPT phase) is ranked as follows: 1250 ^{o}C > 1300 ^{o}C> 1350 ^{o}C > 1150 ^{o}C > AR ≈ 1000 ^{o}C. The pitting corrosion resistance rank from CPT and PREN are not the same, due to different weight factors of the Cr, Mo, and N.

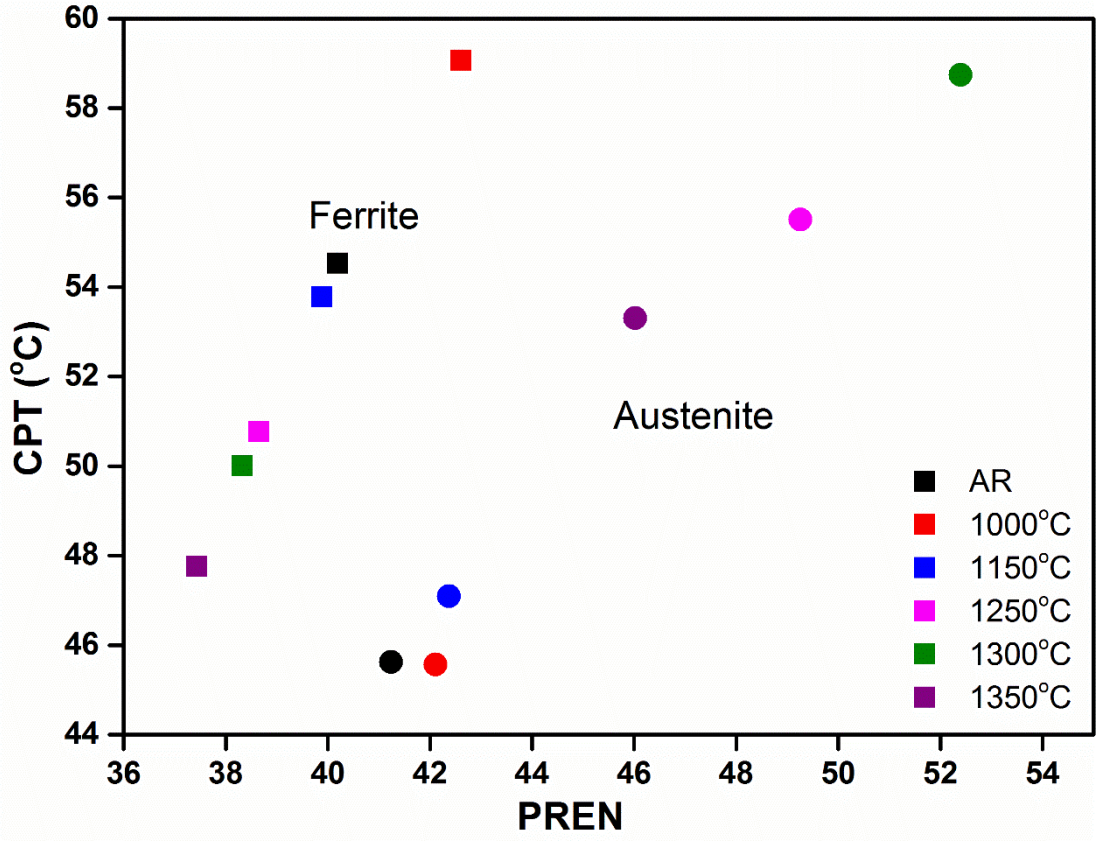

Figure 6 Simulated CPT and PREN values for ferrite and austenite after different solution treatments, with the ferrite shown in squares and the austenite with circles. (CPT = 2.5 × %Cr + 7.6 × %Mo + 31.9 × %N – 41; PREN = %Cr + 3.3 × %Mo+ 30 × %N)

Pitting Corrosion Tests

Figure 7 shows the 3-electrode potentio-dynamic polarisation curves at room temperature for the different annealing treatments. The measured OCP values have minor differences, indicating slightly modified passive film properties. The passive current density response is similar in all samples and remained very low. The current density exceed 0.1 mA/cm^2 at around +0.9 V_{SCE}, but no pits were observed in the experiment. This observation is in line with literature observation where no pits are expected in DSS 2205 in 0.1M HCl at room temperature [42,43]. At higher applied potentials (> +0.9 V_{SCE}) trans-passivity corrosion with oxygen evolution is observed [44].

All polarization studies are summarised in Table 2, with the lowest OCP found after annealing at 1250 ^{o}C. The passive region is estimated via the range of anodic potentials where the current density remains below 0.1 mA/cm^2. The passive current density for specimen annealed at 1350 ^{o}C is slightly higher, which is in line with literature observations [45]. The latter has been attributed to better passive film properties caused by larger grain size sizes [45].

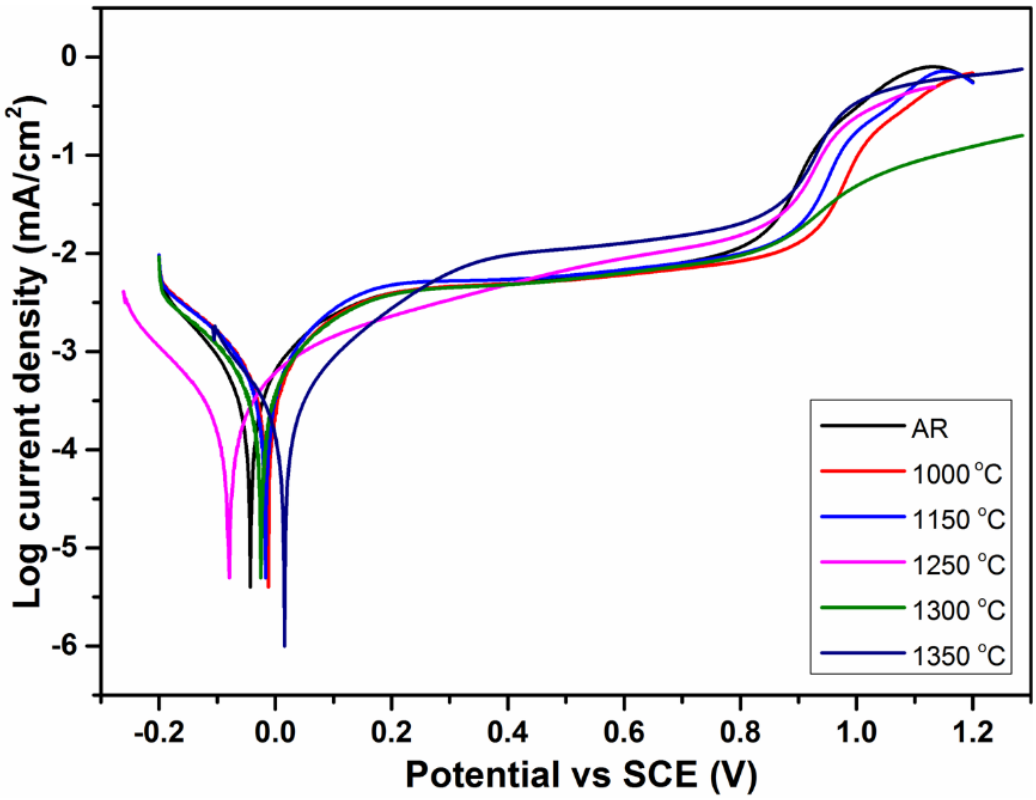

Figure 7 The 3-electrode potentio-dynamic polarisation curves for DSS 2205 at room temperature at different annealed temperature.

Table 2 OCP, passive region, and passive current density obtained for tested specimens after polarization in 0.1M HCl at room temperature.

	OCP (V_{SCE})	Passive region (V_{SCE})	Passive current density (mA/cm^2)
AR	-0.043	0.926	0.011
1000 ^{o}C	-0.012	1.042	0.008
1150 ^{o}C	-0.017	0.987	0.010
1250 ^{o}C	-0.079	1.021	0.012
1300 ^{o}C	-0.025	1.436	0.010
1350 ^{o}C	0.016	1.268	0.044

Bipolar electrochemistry was applied to reveal the localised corrosion resistance of DSS 2205 at room temperature. The methodology for carrying out these tests has been introduced in [30]. Figure 8 (a) gives an optical image of the rectangular BPE surface after testing in 0.1M HCl in the as received condition. Due to the linear potential gradient acting along the BPE, the surface shows different corrosion behaviour as a function of distance to the sample edge. The left side (labelled A) is the oxidation edge, showing crevice corrosion, pitting corrosion, and general corrosion, with the right (labelled C) accommodating the balancing cathodic reactions. Figure 8 (b) gives the pit-covered region of all tested samples with the different annealing treatments. The lengths of the regions containing pits were affected by microstructure, with the difference in length indicating different critical pitting potentials for pit nucleation. All pits on the BPE are open pits, without lacy covers.

1250 ^{o}C heat treatment resulted in pits with predominantly circular-shapes, with higher temperature annealing showing more elliptical shapes, with in parallel localised corrosion at grain boundaries. Pits growing in close proximity to each other or merged pits influence overall pit growth rate, as the local effective applied potential and chloride concentration inside of pits changes [46]. When pit grow close to each other, the cathode area surrounding the pit is reduced, often providing not enough cathodic current to sustain a high pit growth rate [47]. Crevice corrosion is also found at the interface between the resin and sample at the oxidation edge. Crevices typically nucleate at lower applied potentials compared to corrosion pits, which is also observed on the samples in Figure 8 (b).

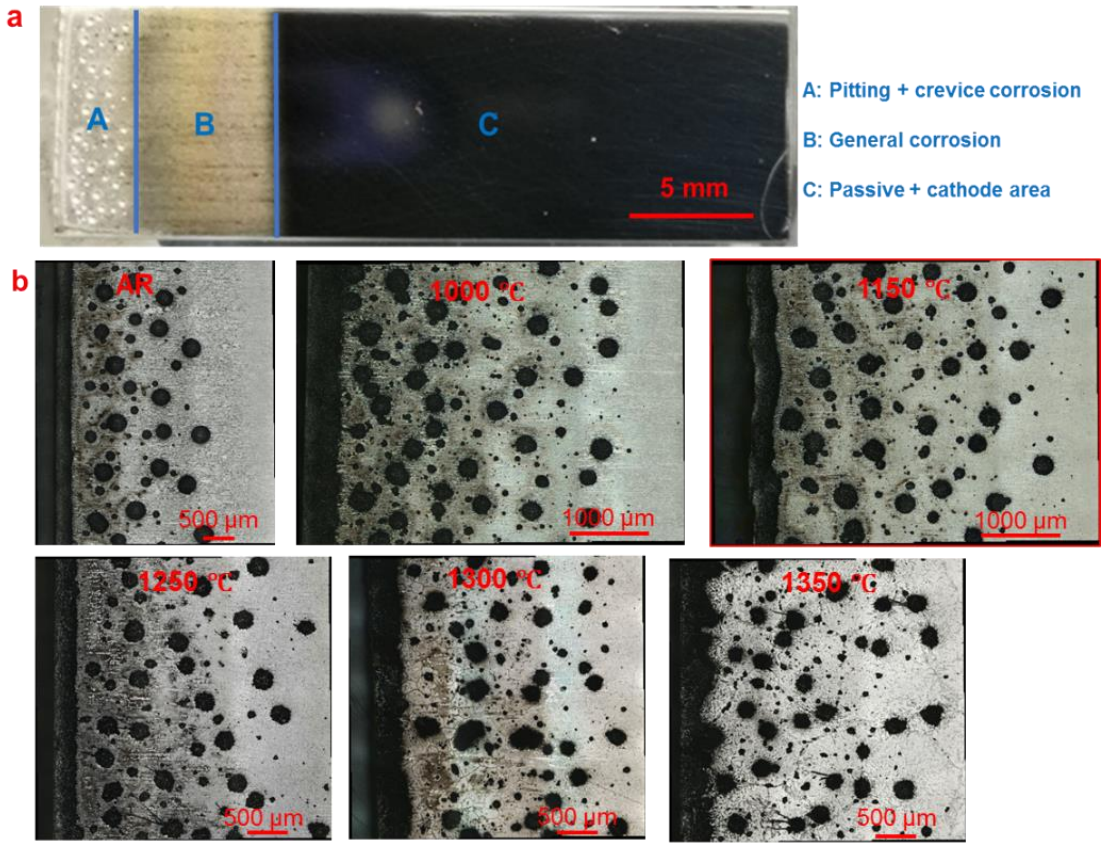

Figure 8 View of the AR DSS 2205 bipolar electrode, outlining the different corrosion regions along the sample surface; (b) higher magnification optical image of the localised corrosion region close to the oxidation edge of all annealing conditions.

Pit Nucleation & Growth

The bipolar treated samples were assessed and inspected in more details. Figure 9 (a) and (b) show two pit nucleation sites, found on samples annealed at 1150 ^{o}C and 1250 ^{o}C. Pit nucleation inside ferrite grain can be seen, with the other site showing pits growing at ferrite–austenite boundaries. Inside the austenite phase, there are no pits. The ferrite phase is preferentially corroding away. Figure 9 (c) gives pit nucleation sites at the ferrite phase, and along a network of grain boundary austenite in the specimen annealed at 1350 ^{o}C, this explains the localised corrosion observed of the BPE at the grain boundary measured in Figure 8 (b) after annealing at 1300 ^{o}C.

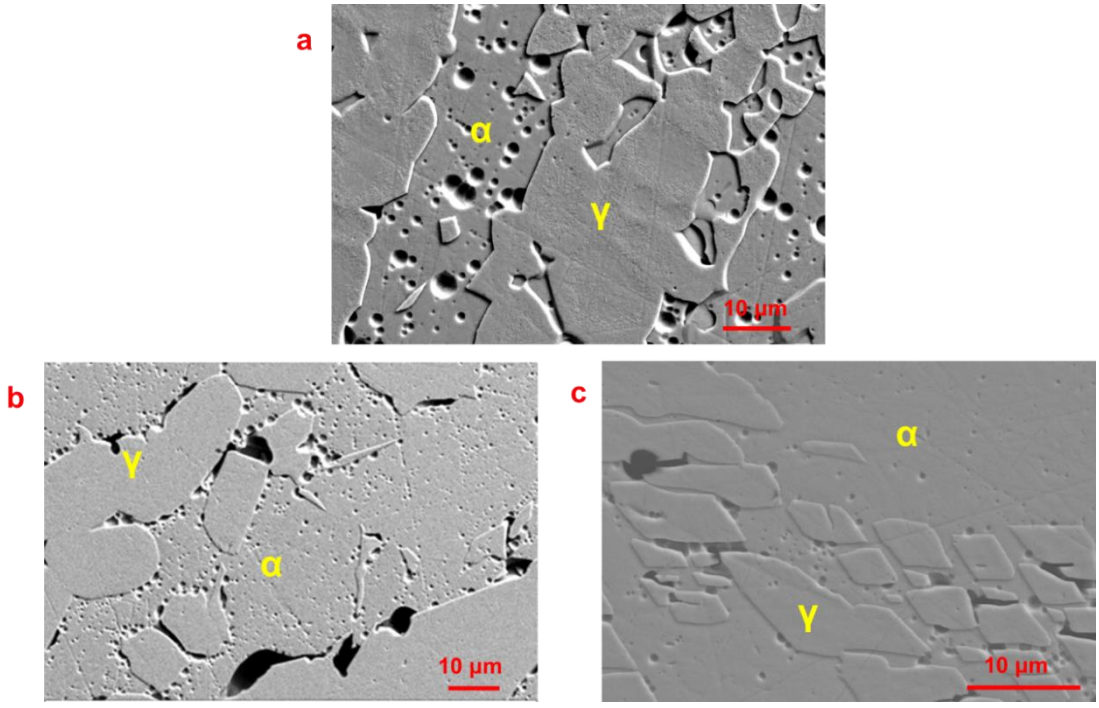

Figure 9 Typical pit nucleation sites at specimens after annealing at (a) 1150 °C and (b) 1250 °C and (c) 1350 °C.

Figure 10 (a) shows a pit grown into the ferrite, with the remaining austenite phase forming a lacy cover. The lacy cover has nearly collapsed, due to the local dissolution of the surrounding ferrite phase. The formation of lacy cover pits in both lean and standard DSS has been observed in previous observations [13,30]. Figure 10 (b) gives a fully-grown pit after consuming the ferrite phase, supporting previous observations that the austenite phase remains unless all the surrounding ferrite is dissolved away. A large sized open pit is highlighted in Figure 10 (c), having a diameter of 60 µm, the edge of the pit shows un-corroded austenite phase remaining with the pit appearing hemi-spherical in shape.

Microstructure changes invoked by annealing heat treatments influences metastable pit growth. After the pit grows to a large hemi-spherical size, it becomes independent to the microstructure, as the ferrite and austenite size is small compared to the overall pit mouth. Slightly elongated pit is present after

annealing at 1300 ºC, which is in turn related to the large size of the ferrite grains. The ferrite size also influences the shape and morphology of the lacy covers, which then affects the pit growth kinetics by affecting the ion exchange from inside the pit to the outside bulk electrolyte [13]. All heat treated DSS 2205 microstructures showed pits nucleating at the interface between ferrite and austenite or inside the ferrite phase, with pit growth via consuming the ferrite phase.

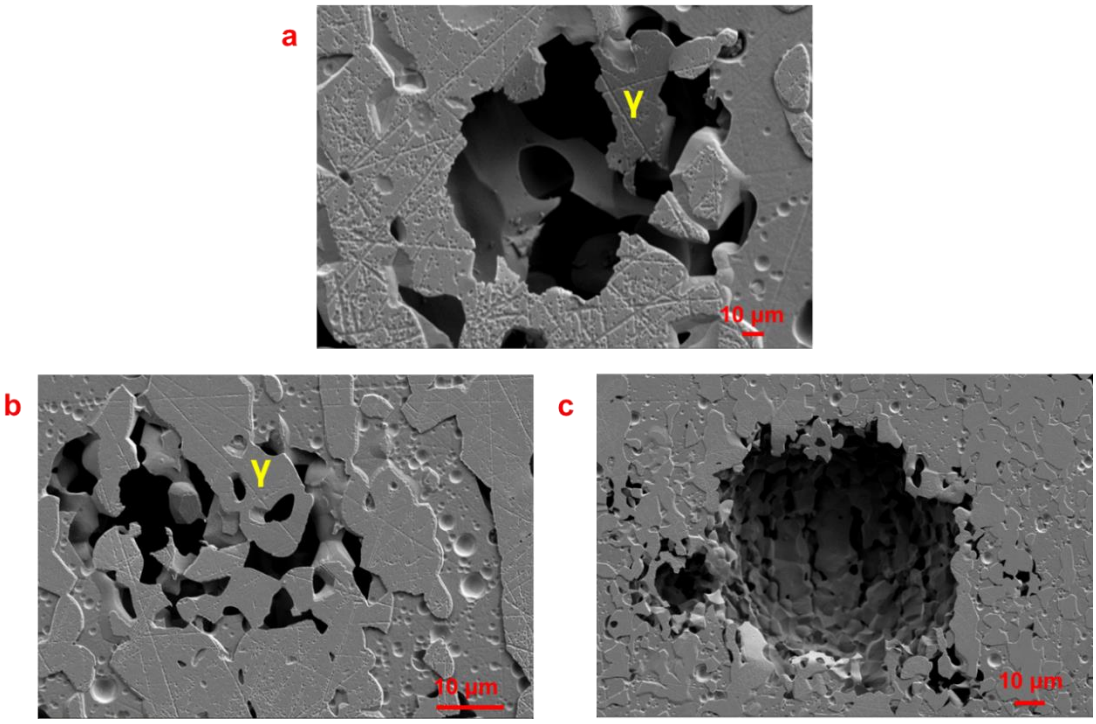

Figure 10 The pitting propagation for the specimen annealed at 1000 ºC.

Pit Shape and Morphology

The pit depth measured via confocal microscopy is correlated to the overall pit volume of each pit in Figure 11 (a-c) for all different annealed temperatures. Equation 1 and 2 are introduced to provide an estimate of the measured pit shape. Equation 1 assumes a perfectly hemi-spherical shape, when the depth (d) is the same value as the radius (r).

The pit depth and volume of each pit are then compared to different shape factors (α = 0.5, 1, 2), which is reflected by the three reference curves shown in Figure 11. If we keep the pit depth (d) constant, these curves are then indicative of either wide and shallow pits (α = 0.5; e.g. the radius is twice the depth), perfectly hemispherical pits (α = 1), or deep and narrow pits (α = 2; where the radius is half the depth).

$$V = \frac{1}{2} \times \frac{4}{3} \times \pi \times d \times r^2 \qquad \textbf{Equation 1}$$

$$d = \alpha x r^2 \qquad \textbf{Equation 2}$$

All pits are chiefly concentrated at two different depths; one group is less than 40 μm deep, and the other depth group is over 100 μm deep. It seems that a pit depth of 40 μm may act as the critical threshold parameter for the development of metastable to stable pits. Stable pits have a large pit volume/depth ratio which act as diffusion barrier.

Figure 11 (b) shows the pit shape with pit depth less than 40 μm; the smaller pits show a nice trend from "wide" (as received) to more a narrow shape with higher annealing temperature. This is related to grain size and the ferrite-austenite ratio in DSS [48,49]. For example, the pit growth in DSS 2205 is found to grow more in depth, but in DSS 2202 pits grow along the surface [50]. Figure 11 (c) shows the pit shape when pit depth > 100 μm, the larger pits also show a very nice trend with higher annealing temperature slightly deeper pits, but they become more semi-circular than smaller pits. For the specimen annealing at 1350 ^{o}C, the pits shape is the same for small and large pits. The maximum pit depth is increasing with higher annealing temperature up to 1250 ^{o}C, then the maximum pit depth becomes constant. The maximum pit depth becomes similar after annealing over 1250 ^{o}C, as the formation of austenite inside and at the grain boundary of the ferrite. The effect of austenite acts as a barrier to reduce the pit growth kinetics and the nitrogen loss to increase the pit growth kinetics are cancelled.

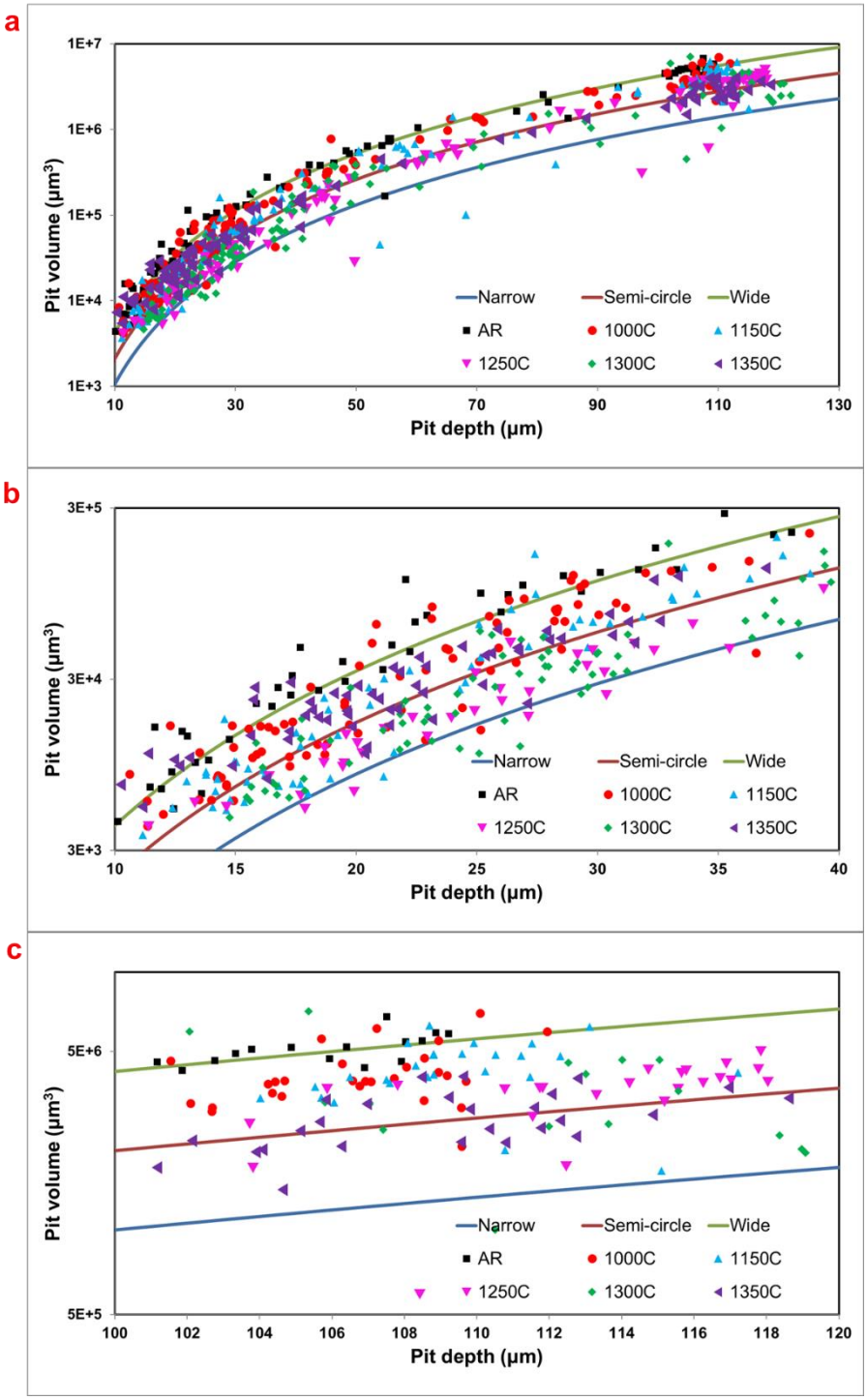

Figure 11 (a) Pit depth and the corresponding volume on the BPE with different annealed temperature. With the pit shape of (b) pit depth from 10-40 µm and (c) pit depth from 100 – 120 µm.

Comparison & Optimisation

Figure 12 (a) gives the overall pit volume vs pit covered length for each heat treatment condition. A longer pit covered length indicates a lower critical pitting potential, so higher susceptibility. The shortest pit covered region is measured in the AR condition (2.5 mm). For specimen annealed at 1000 ^{o}C, the pit covered length reaches the maximum ≈ 4.4 mm. Then continues reducing to 3.1mm for specimen annealed at 1250 ^{o}C. From specimen annealing over 1300 ^{o}C, the pit covered length increases from 3.1 mm to 3.5 mm. A larger pit volume indicates a higher pit growth kinetics, even the pit growth in the depth direction is potential independent, but the overall pit volume is related to the applied potential [30]. The pit volume increases from AR to annealed at 1000 ^{o}C, then reduces with higher annealed temperatures. The pitting corrosion resistance is AR > 1250 ^{o}C > 1300 ^{o}C > 1350 ^{o}C > 1150 ^{o}C > 1000 ^{o}C from the pit covered length on the BPE. But the rank for the pit growth kinetics is different, which is 1000 ^{o}C > 1150 ^{o}C > 1250 ^{o}C ≈ AR > 1300 ^{o}C > 1350 ^{o}C.

Figure 12 (b) displays the overall pit volume vs PREN values, indicating that smaller pit volumes have a lower PREN. This is opposite to higher PREN indicating a higher pit corrosion resistance, because PREN is only used to estimate the critical pitting potential, which cannot used to estimate the pit growth kinetics. The rank of the pitting resistance from the critical pitting potential and pit volume is not the same, as the nitrogen give a more contribution effect to the pit growth kinetics and size/shape of ferrite/austenite also affect the pit growth kinetics. N reduces the pit growth kinetics, as N increases the pH value inside of pit electrolyte from reach with H^{+} to form NH_3 and NH_4^{+} [51]. The pit growth kinetics also run for 900 seconds, but the pit nucleation time is less than 15 seconds [30], so the nitrogen influence the pit growth kinetics for a longer time. The shape of austenite and ferrite is also an important factor for pit growth rate, as only ferrite is corroded away, so the remained austenite can act as a wall to reduce the pit growth. The specimen

after annealing over 1300 ^{o}C has the grain boundary austenite which can reduce the pit growth kinetics even with a more nitrogen loss condition.

Interestingly, specimens annealed at 1000 ^{o}C have a ratio of ferrite and austenite of 50:50, but the corrosion resistance is the lowest. In contrast, the highest difference in alloying elements exists in this microstructure between ferrite and austenite (Figure 3b), so the galvanic effect between the phases may accelerate the corrosion rate. For the specimen heat-treated over 1300 ^{o}C, the critical pitting potential increases. The possible reason is the concentration of ferrite and elements distribution, the critical current to nucleate pitting corrosion need a higher applied potential due to a large concentration of ferrite, and the alloying elements between the ferrite and austenite is more homogenous, so the galvanic corrosion between the two phases is very small, which cannot enhance the corrosion rate.

Figure 12 clearly shows differences of the initiation behaviour via the pit covered length with pit growth information supported by the overall dissolved pit volume. With this in mind, all high temperature treatments seem to have smaller dissolved volumes, with the as received material providing the highest resistance against pit nucleation. These results demonstrate the application of bipolar electrochemistry for assessing, comparing, and ranking the localised corrosion performance of duplex stainless steel at room temperature. Key for optimising the corrosion resistance seems to be related to the chemical signature of both crystallographic phases, and in particular their interplay. This observation provides the means for developing microstructures with improved resistance to pit growth.

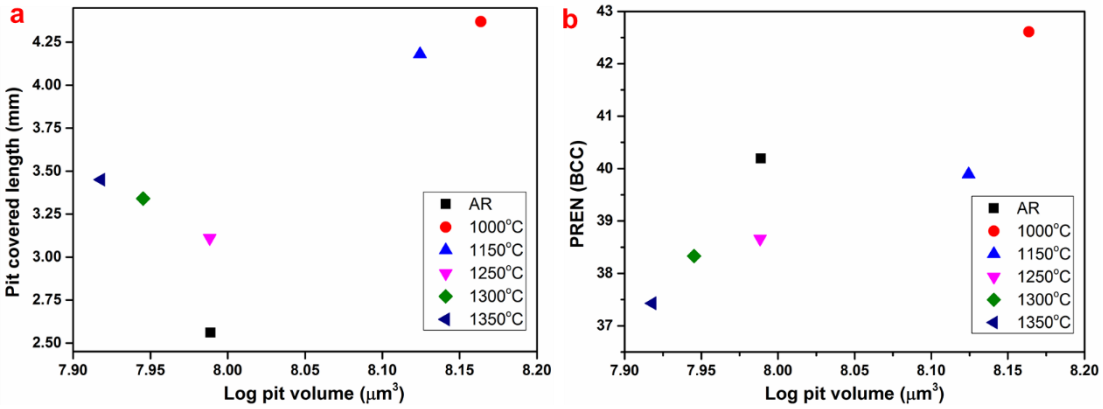

Figure 12 (a) the pit covered length and (b) PREN of ferrite phase vs the overall dissolved pit volume.

Conclusions

The volume of ferrite increases with higher annealing temperatures, but the difference in galvanic behaviour between ferrite and austenite reduces significantly.

The element distribution affected the pit growth behaviour, with the lowest dissolved pit volume observed on samples with the lowest difference in chemical composition of both phases.

Corrosion pits nucleated within ferrite and the interface between ferrite and austenite.

The critical pitting potential, pit growth kinetics, and pit shapes changed with solution treatments, and the rank of critical pitting potential/temperature is not the same when assessed with PREN, CPT, and bipolar electrochemistry.

Bipolar electrochemistry was for the first time successfully applied to assess and rank duplex 2205 microstructure characteristics at room temperature.

Data availability

The raw/processed data required to reproduce these findings cannot be shared at this time as the data also forms part of an ongoing study.

CRediT authorship contribution statement

Yiqi Zhou: Conceptualization, Methodology, Validation, Formal analysis, Investigation, Data curation, Writing - original draft, Visualization, Funding acquisition.

Dirk L Engelberg: Conceptualization, Methodology, Validation, Formal analysis, Investigation, Funding acquisition, Writing - review and editing, Supervision.

Declaration of Competing Interest

The authors declare that they have no known competing financial interests or personal relationships that could have appeared to influence the work reported in this paper.

Acknowledgements

The authors acknowledge the support of the Henry Royce Institute for access to the Keyence laser scanning confocal microscope and the ZEISS Sigma FEG-SEM at Royce@Manchester (EP/R00661X/1).

References

[1] H. Tan, Z. Wang, Y. Jiang, D. Han, J. Hong, L. Chen, L. Jiang, J. Li, Annealing temperature effect on the pitting corrosion resistance of plasma arc welded joints of duplex stainless steel UNS S32304 in 1.0M NaCl, Corros. Sci. 53 (2011) 2191–2200. https://doi.org/10.1016/j.corsci.2011.02.041.

[2] J. Nilsson, Overview Super duplex stainless steels, Mater. Sci. Technol. 8 (1992) 685–700. https://doi.org/10.1179/mst.1992.8.8.685.

[3] S.T. Kim, S.H. Jang, I.S. Lee, Y.S. Park, Effects of solution heat-treatment and nitrogen in shielding gas on the resistance to pitting corrosion of hyper duplex stainless steel welds, Corros. Sci. 53 (2011) 1939–1947. https://doi.org/10.1016/j.corsci.2011.02.013.

[4] J.H. Potgieter, P.A. Olubambi, L. Cornish, C.N. Machio, E.S.M. Sherif, Influence of nickel additions on the corrosion behaviour of low nitrogen 22% Cr series duplex stainless steels, Corros. Sci. 50 (2008) 2572–2579. https://doi.org/10.1016/j.corsci.2008.05.023.

[5] Z. Zhang, Z. Wang, Y. Jiang, H. Tan, D. Han, Y. Guo, J. Li, Effect of post-weld heat

treatment on microstructure evolution and pitting corrosion behavior of UNS S31803 duplex stainless steel welds, Corros. Sci. 62 (2012) 42–50. https://doi.org/10.1016/j.corsci.2012.04.047.

[6] G.S. Frankel, Pitting corrosion of metals a review of the critical factors, J. Electrochem. Soc. 145 (1998) 2186–2198. https://doi.org/10.5006/0010-9312-19.8.261.

[7] S.M. G.Burstein, P.Pistorius, Evaluating the critical chemistry for repassivation at the corroding surface using mass transport model-based artificial pit experiments, Corros. Sci. 35 (1993) 57–62. https://doi.org/10.1016/0010-938X(93)90133-2.

[8] J. Srinivasan, R.G. Kelly, Evaluating the critical chemistry for repassivation at the corroding surface using mass transport model-based artificial pit experiments, J. Electrochem. Soc. 163 (2016) C768–C777. https://doi.org/10.1149/2.0661613jes.

[9] J. Srinivasan, C. Liu, R.G. Kelly, Geometric evolution of flux from a corroding one-dimensional pit and its implications on the evaluation of kinetic parameters for pit stability, J. Electrochem. Soc. 163 (2016) C694–C703. https://doi.org/10.1149/2.1221610jes.

[10] P. Ernst, R.C. Newman, Pit growth studies in stainless steel foils. I. Introduction and pit growth kinetics, Corros. Sci. 44 (2002) 927–941. https://doi.org/10.1016/S0010-938X(01)00133-0.

[11] W. Tian, S. Li, N. Du, S. Chen, Q. Wu, Effects of applied potential on stable pitting of 304 stainless steel, Corros. Sci. 93 (2015) 242–255. https://doi.org/10.1016/j.corsci.2015.01.034.

[12] B. Deng, Y. Jiang, J. Gong, C. Zhong, J. Gao, J. Li, Critical pitting and repassivation temperatures for duplex stainless steel in chloride solutions, Electrochim. Acta. 53 (2008) 5220–5225. https://doi.org/10.1016/j.electacta.2008.02.047.

[13] K. Eguchi, T.L. Burnett, D.L. Engelberg, X-Ray tomographic characterisation of pitting corrosion in lean duplex stainless steel, Corros. Sci. 165 (2019) 108406. https://doi.org/10.1016/j.corsci.2019.108406.

[14] H.Y. Ha, M.H. Jang, T.H. Lee, J. Moon, Interpretation of the relation between ferrite fraction and pitting corrosion resistance of commercial 2205 duplex stainless steel, Corros. Sci. 89 (2014) 154–162. https://doi.org/10.1016/j.corsci.2014.08.021.

[15] L. F. Garfias-Mesias, J. M. Sykes, C. D. S. Tuck, The effect of phase compositions on the pitting corrosion of 25 Cr duplex stainless steel in chloride solutions, Corros. Sci. 38 (1996) 1319–1330.

[16] L.Q. Guo, M. Li, X.L. Shi, Y. Yan, X.Y. Li, L.J. Qiao, Effect of annealing temperature on the corrosion behavior of duplex stainless steel studied by in situ techniques, Corros. Sci. 53 (2011) 3733–3741. https://doi.org/10.1016/j.corsci.2011.07.019.

[17] N. Lopez, M. Cid, M. Puiggali, Influence of σ-phase on mechanical properties and

corrosion resistance of duplex stainless steels, Corros. Sci. 41 (1999) 1615–1631. https://doi.org/10.1016/S0010-938X(99)00009-8.

[18] P. Reccagni, L.H. Guilherme, Q. Lu, M.F. Gittos, D.L. Engelberg, Reduction of austenite-ferrite galvanic activity in the heat-affected zone of a Gleeble-simulated grade 2205 duplex stainless steel weld, Corros. Sci. 161 (2019). https://doi.org/10.1016/j.corsci.2019.108198.

[19] S. Kim, S. Kim, I. Lee, Y. Park, M. Shin, Y. Kim, Effects of shielding gases on the microstructure and localized corrosion of tube-to-tube sheet welds of super austenitic stainless steel for seawater cooled condenser, Corros. Sci. 53 (2011) 2611–2618. https://doi.org/10.1016/j.corsci.2011.04.021.

[20] L. Zhang, W. Zhang, Y. Jiang, B. Deng, D. Sun, J. Li, Influence of annealing treatment on the corrosion resistance of lean duplex stainless steel 2101, Electrochim. Acta. 54 (2009) 5387–5392. https://doi.org/10.1016/j.electacta.2009.04.023.

[21] R.A. Perren, T. Suter, C. Solenthaler, G. Gullo, P.J. Uggowitzer, H. Böhni, M.O. Speidel, Corrosion resistance of super duplex stainless steels in chloride ion containing environments: Investigations by means of a new microelectrochemical method. II. Influence of precipitates, Corros. Sci. 43 (2001) 727–745. https://doi.org/10.1016/S0010-938X(00)00088-3.

[22] E. Angelini, B. De Benedetti, F. Rosalbino, Microstructural evolution and localized corrosion resistance of an aged superduplex stainless steel, Corros. Sci. 46 (2004) 1351–1367. https://doi.org/10.1016/j.corsci.2003.09.024.

[23] Z. Wei, J. Laizhu, H. Jincheng, S. Hongmei, Effect of ageing on precipitation and impact energy of 2101 economical duplex stainless steel, Mater. Charact. 60 (2008) 50–55. https://doi.org/10.1016/j.matchar.2008.07.002.

[24] K. Eguchi, T.L. Burnett, D.L. Engelberg, X-ray tomographic observation of environmental assisted cracking in heat-treated lean duplex stainless steel, Corros. Sci. 184 (2021) 109363. https://doi.org/10.1016/j.corsci.2021.109363.

[25] N. Pébère, V. Vivier, Local electrochemical measurements in bipolar experiments for corrosion studies, ChemElectroChem. 3 (2016) 415–421. https://doi.org/10.1002/celc.201500375.

[26] S. Munktell, L. Nyholm, F. Björefors, Towards high throughput corrosion screening using arrays of bipolar electrodes, J. Electroanal. Chem. 747 (2015) 77–82. https://doi.org/10.1016/j.jelechem.2015.04.008.

[27] S. Munktell, M. Tydén, J. Högström, L. Nyholm, F. Björefors, Bipolar electrochemistry for high-throughput corrosion screening, Electrochem. Commun. 34 (2013) 274–277. https://doi.org/10.1016/j.elecom.2013.07.011.

[28] Y. Zhou, D.L. Engelberg, Application of a modified bi-polar electrochemistry approach

to determine pitting corrosion characteristics, Electrochem. Commun. 93 (2018) 158–161. https://doi.org/10.1016/j.elecom.2018.06.013.

[29] Y. Zhou, A. Kablan, D.L. Engelberg, Metallographic screening of duplex stainless steel weld microstructure with a bipolar electrochemistry technique, Mater. Charact. 169 (2020) 110605. https://doi.org/10.1016/j.matchar.2020.110605.

[30] Y. Zhou, D.L. Engelberg, Fast testing of ambient temperature pitting corrosion in type 2205 duplex stainless steel by bipolar electrochemistry experiments, Electrochem. Commun. 117 (2020). https://doi.org/10.1016/j.elecom.2020.106779.

[31] Y. Zhou, D.L. Engelberg, On the Application of Bipolar Electrochemistry to Characterise the Localised Corrosion Behaviour of Type 420 Ferritic Stainless Steel, Metals (Basel). 10 (2020) 794. https://doi.org/10.3390/met10060794.

[32] Y. Zhou, N. Stevens, D. Engelberg, Corrosion electrochemistry with a segmented array bipolar electrode, Electrochim. Acta. 375 (2021) 137668. https://doi.org/10.1016/j.electacta.2020.137668.

[33] Y. Zhou, S. Mahmood, D. Engelberg, Brass dezincification with a bipolar electrochemistry technique, Surfaces and Interfaces. 22 (2021) 100865. https://doi.org/10.1016/j.surfin.2020.100865.

[34] Y. Zhou, J. Qi, D.L. Engelberg, On the application of bipolar electrochemistry for simulating galvanic corrosion behaviour of dissimilar stainless steels, Electrochem. Commun. 126 (2021) 107023. https://doi.org/10.1016/j.elecom.2021.107023.

[35] Y. Zhou, D. Engelberg, Accessing the full spectrum of corrosion behaviour of tempered type 420 stainless steel, Mater. Corros. (2021) 1–12. https://doi.org/10.1002/maco.202112442.

[36] S. Aa, F.F. Figure, G. If, The effect of high-temperature exposure on the microstructural stability and toughness property in a 2205 duplex stainless steel, Mater. Sci. Eng. A. 338 (2002) 259–270. https://doi.org/10.1016/S0921-5093(02)00093-X.

[37] H. Tan, Y. Jiang, B. Deng, T. Sun, J. Xu, J. Li, Effect of annealing temperature on the pitting corrosion resistance of super duplex stainless steel UNS S32750, Mater. Charact. 60 (2009) 1049–1054. https://doi.org/10.1016/j.matchar.2009.04.009.

[38] Y. Zhang, F. Cheng, S. Wu, Improvement of pitting corrosion resistance of wire arc additive manufactured duplex stainless steel through post-manufacturing heat-treatment, Mater. Charact. (2020) 110743. https://doi.org/10.1016/j.matchar.2020.110743.

[39] K. Vijayalakshmi, V. Muthupandi, R. Jayachitra, Influence of heat treatment on the microstructure,ultrasonic attenuation and hardness of SAF 2205 duplex stainless steel, Mater. Sci. Eng. A. 529 (2011) 447–451.

https://doi.org/10.1016/j.msea.2011.09.059.

[40] C. David, F. Ruel, F. Krajcarz, C. Boissy, S. Saedlou, V. Vignal, Effect of grain size on the anodic dissolution of lean duplex UNS S32202 austenitic-ferritic stainless steel, Corrosion. 75 (2019) 1450–1460. https://doi.org/10.5006/3218.

[41] V.A. Hosseini, S. Wessman, K. Hurtig, L. Karlsson, Nitrogen loss and effects on microstructure in multipass TIG welding of a super duplex stainless steel, Mater. Des. 98 (2016) 88–97. https://doi.org/10.1016/j.matdes.2016.03.011.

[42] N. Ebrahimi, M.H. Moayed, A. Davoodi, Critical pitting temperature dependence of 2205 duplex stainless steel on dichromate ion concentration in chloride medium, Corros. Sci. 53 (2011) 1278–1287. https://doi.org/10.1016/j.corsci.2010.12.019.

[43] M. Adeli, M.A. Golozar, K. Raeissi, Pitting corrosion of SAF2205 duplex stainless steel in acetic acid containing bromide and chloride, Chem. Eng. Commun. 197 (2010) 1404–1416. https://doi.org/10.1080/00986441003626151.

[44] C. Örnek, M. Långberg, J. Evertsson, G. Harlow, W. Linpé, L. Rullik, F. Carlà, R. Felici, E. Bettini, U. Kivisäkk, E. Lundgren, J. Pan, In-situ synchrotron GIXRD study of passive film evolution on duplex stainless steel in corrosive environment, Corros. Sci. 141 (2018) 18–21. https://doi.org/10.1016/j.corsci.2018.06.040.

[45] X.Y. Wang, D.Y. Li, Mechanical and electrochemical behavior of nanocrystalline surface of 304 stainless steel, Electrochim. Acta. 47 (2002) 3939–3947. https://doi.org/10.1016/S0013-4686(02)00365-1.

[46] N.J. Laycock, D.P. Krouse, S.C. Hendy, D.E. Williams, Computer simulation of pitting corrosion of stainless steels, Interface, Electrochem. Soc. (2014) 65–71. https://doi.org/10.1149/2.F05144IF.

[47] M.T. Woldemedhin, M.E. Shedd, R.G. Kelly, Evaluation of the maximum pit size model on stainless steels under thin film electrolyte conditions, J. Electrochem. Soc. 161 (2014) E3216–E3224. https://doi.org/10.1149/2.023408jes.

[48] H.J. Sussmann, Understanding why PREN alone cannot be used to select duplex stainless steels, in: NACE Int. Conf., 2015: pp. 1–10.

[49] H. Hwang, Y. Park, Effects of heat treatment on the phase ratio and corrosion resistance of duplex stainless steel, Mater. Trans. 50 (2009) 1548–1552. https://doi.org/10.2320/matertrans.MER2008168.

[50] C. Örnek, F. Léonard, S.A. McDonald, A. Prajapati, P.J. Withers, D.L. Engelberg, Time-dependent in situ measurement of atmospheric corrosion rates of duplex stainless steel wires, Npj Mater. Degrad. 2 (2018) 1–15. https://doi.org/10.1038/s41529-018-0030-9.

[51] R.F.A. Jargelius-Pettersson, Electrochemical investigation of the influence of nitrogen alloying on pitting corrosion of austenitic stainless steels, Corros. Sci. 41 (1999) 1639–

1664. https://doi.org/10.1016/S0010-938X(99)00013-X.